

Research Article

Int J Energy Studies 2024; 9(3): 493-517

DOI: 10.58559/ijes.1467215

Received : 09 Apr 2024

Revised : 08 July 2024

Accepted : 12 Aug 2024

A full-scale CFD model of scavenge air inlet temperature on two-stroke marine diesel engine combustion and exhaust emission characteristics

Enes Fatih Pehlivan^{a*}, İsmail Altın^b

^aOrdu University, Fatsa Faculty of Marine Sciences, Department of Naval Architecture and Marine Engineering, Fatsa, Ordu, Turkey, ORCID: 0000-0003-4956-1098

^bKaradeniz Technical University, Sürmene Faculty of Marine Sciences, Department of Naval Architecture and Marine Engineering, Sürmene, Trabzon, Turkey, ORCID: 0000-0002-7587-9537

(*Corresponding Author: enespehlivan@odu.edu.tr)

Highlights

- A numerical model of a two-stroke marine diesel engine was developed and validated.
- The effects of scavenge air inlet temperature on engine performance and exhaust emissions were investigated.
- The maximum cylinder pressure decreases in 5.58 % with the increase in scavenge air inlet temperature.
- The exhaust emissions increase as scavenge air inlet temperature rises.

You can cite this article as: Pehlivan EF, Altın İ. A full-scale CFD model of scavenge air inlet temperature on two-stroke marine diesel engine combustion and exhaust emission characteristics. Int J Energy Studies 2024; 9(3): 493-517.

ABSTRACT

Most ships in the maritime transport sector are equipped with large two-stroke marine diesel engines in their propulsion systems. Therefore, ensuring stable and long-term operation of these engines is crucial to maintaining freight transportation. The design of the ship's machinery, particularly the diesel engine, is a crucial step in achieving this goal. Computational Fluid Dynamics (CFD) tools can be used to achieve this goal. This article presents a full-scale CFD study on the effect of different scavenge air inlet temperatures (300, 312, 330 and 340 K) on the combustion process and generation of exhaust emissions in a two-stroke marine diesel engine using ANSYS Forte software. Regarding the cylinder pressure, the presented model agrees well with experimental data. The maximum cylinder pressure decreases as the scavenge air inlet temperature increases, whereas the maximum cylinder temperature increases as the scavenge air inlet temperature increases. The maximum NO_x, CO and UHC emission values are calculated to be 2256.5, 20375.8 and 3743.9 ppm, respectively, at a scavenge air inlet temperature of 340 K. Due to the higher combustion temperature caused by the increasing scavenge air inlet temperature, it is observed that the exhaust emission levels increase.

Keywords: Two-stroke marine diesel engine, Scavenge air inlet temperature, CFD model, Combustion, Exhaust emission.

1. INTRODUCTION

The global economy heavily relies on the shipping industry, which is responsible for nearly 90% of the transportation in international trade [1]. Ocean-going commercial vessels (OCVs), which are primarily used for long-distance transportation of global commodities, typically employ two-stroke marine diesel engines (MDEs) [2]. These engines are preferred over four-stroke diesel engines used in high- and medium-speed ships due to their efficiency, high power-to-weight ratio, cost-effectiveness, and reliability [3, 4]. In this context, research studies regarding two-stroke MDEs are of great importance due to the high economic benefits and long-term environmental advantages of MDEs [5]. Innovative engine design, scavenging process, combustion analysis, and exhaust emissions have been considered as the main topics of research in two-stroke MDEs' studies. One of methods employed to investigate research topics in two-stroke MDE's studies is Computational Fluid Dynamics (CFD) analysis. CFD analysis has emerged as a powerful tool for investigating various aspects of engine performance, combustion, emissions, and efficiency [6]. The utilization of CFD simulations allows researchers to delve deep into the intricate processes occurring within two-stroke MDEs, providing valuable insights that can inform design improvements and optimization strategies [7, 8].

In the realm of literature, CFD simulations have emerged as a pivotal tool for the analysis and optimization of two-stroke MDEs. Several studies have highlighted the significance of CFD models in understanding various aspects of two-stroke MDEs. Chryssakis et al. [9] developed a two-stroke diesel engine 3D model using the KIVA-3V code to examine the effects of two water injection strategies (fumigation and direct water injection (DWI) techniques) on the NO_x emissions. The results show that DWI method is an effective way to reduce NO_x emissions and meets International Maritime Organization (IMO) standards (i.e., 80% reduction). Liu et al. [10] performed a multi-dimensional numerical simulations to identify feasible strategies for meeting the Tier III regulations and to evaluate the effect of the Miller cycle, high compression ratio with exhaust gas recirculation (EGR), and water-emulsified fuel (WEF) on NO_x emission and fuel economy in a low-speed two-stroke MDE. The findings indicated that EGR had the potential to meet Tier III regulations of the IMO when it combined with WEF. Yang et al. [11] developed a CFD model using ANSYS Fluent software for a large marine two-stroke dual fuel engine with high-pressure gaseous fuel direct injection. The study compared combustion phenomena between gas and diesel modes at 75% load, revealing that gas mode combustion occurs at lower maximum temperatures and leaner conditions, resulting in reduced NO_x emissions. Faming and Jin [5] used

the CFD software ANSYS FLUENT to simulate the scavenging process of a large two-stroke MDE. The results from the simulation were compared with shop test data, and the study provides a reference for using CFD in optimizing the scavenging process of such engines. This study emphasizes the importance of CFD in the research and development of large two-stroke MDEs, underlining its pivotal role in advancing engine technology. Senčić et al. [12] developed a CFD model using OpenFOAM open-source software and validated it by comparing simulation results with experimental data. They analyzed the influence of various operational parameters on the scavenging efficiency. The study found that scavenging efficiency decreases with engine load and increases with the pressure difference between the exhaust and scavenging port. The main idea of the article is the importance of CFD simulations in optimizing the scavenging process in large two-stroke MDEs. Mavrelou and Theotokatos [13] developed a numerical model to investigate and optimize the engine settings of large marine two-stroke dual fuel engines. The study performed a parametric investigation to identify settings that can optimize the engine operation in terms of CO₂ and NO_x emissions trade-off. The results indicate that CO₂ and NO_x emissions can be simultaneously reduced. However, optimizing the engine in the high load region is challenging due to the permissible cylinder pressure constraint.

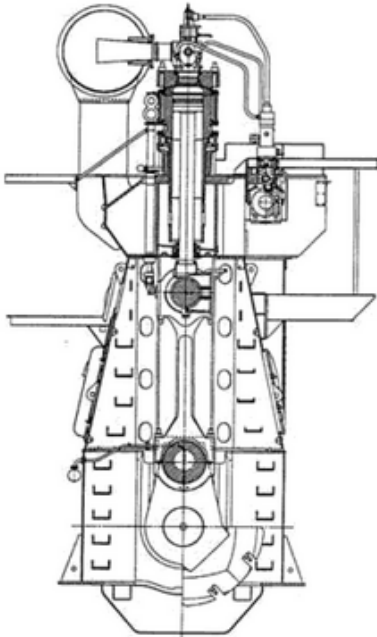
Upon reviewing the existing literature, there are numerous studies based on computational fluid dynamics approaches related to the scavenging process in large two-stroke marine diesel engines. However, in these studies, the geometry used in the analysis is generally preferred as sector geometry to shorten the computation time. Therefore, in this study, a numerical analysis was performed with a computational fluid dynamics approach by creating a geometry that includes the scavenging and exhaust port of the MDE. The purpose of this study is to carry out comprehensive viewpoints of CFD modeling study of a two-stroke MDEs in detail. The novelty of this study is the examination of performance and exhaust emission characteristics by performing a full-scale cycle analysis of a MDE.

2. METHODOLOGY

2.1. Description of the Two-Stroke Marine Diesel Engine

In this research, a large two-stroke MDE was used for numerical simulations is derived from the data of the MAN Diesel & Turbo A/S 4T50MX test engine, housed at the research facility [14]. All specifications of the test engine are given in Table 1.

Table 1. Specifications of the 4T50MX marine diesel engine at full load conditions [14,15].

Cylinder number	4	
Engine output	7500 kW	
Bore	500 mm	
Stroke	2200 mm	
Connecting rod length	2885 mm	
Compression ratio	17.28	
Compression volume	0.02653 m ³	
Engine speed	123 rpm	
Exhaust valve diameter (d_{ev})	0.27 m	
Number of scavenge ports (n_{port})	30	
Scavenge port height (h_p)	0.21 m	
Scavenge port width (w_p)	0.04 m	
Scavenge port depth (l_p)	0.05 m	
Scavenge port angle (θ_{sc})	20°	

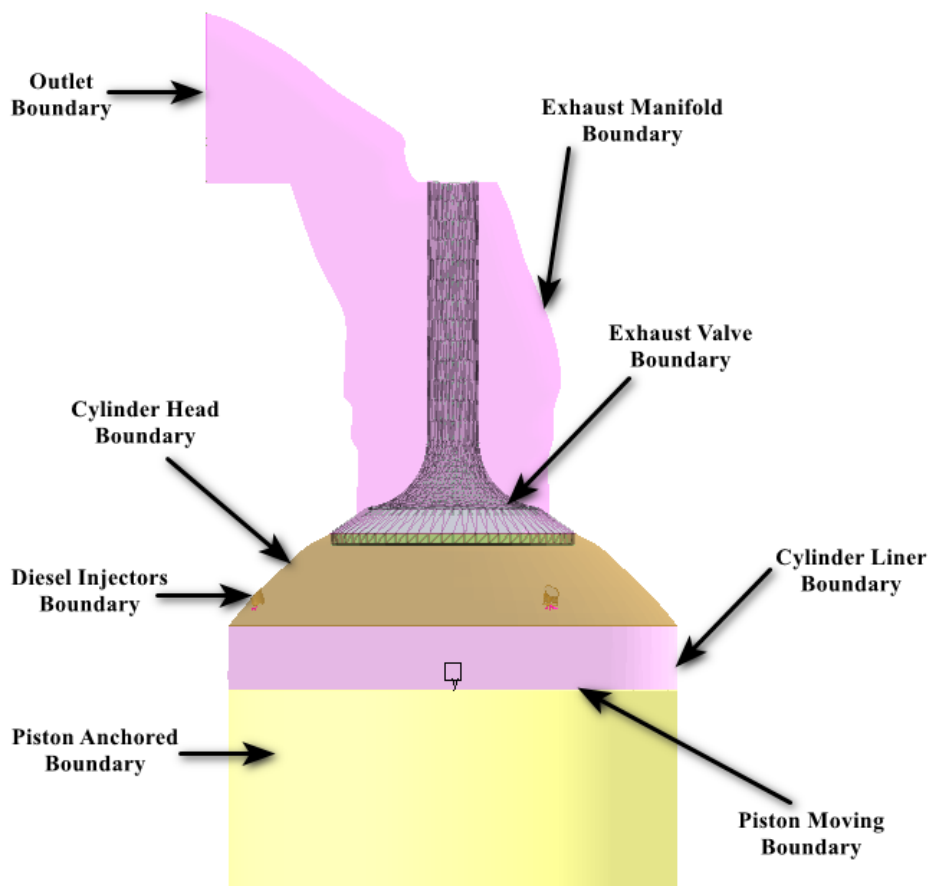
To validate the in-cylinder pressure predicted by the CFD model, experimental in-cylinder pressure is utilized. The pressure is gauged at a specific location on the cylinder cover. From the bottom dead center (BDC) to the point of exhaust valve closure (EVC), the pressure remains nearly constant since both the scavenging ports and the exhaust valve are open. From EVC to the top dead center (TDC), there is a rise in pressure due to compression until it reaches TDC. Upon fuel injection and subsequent combustion, there is an increase in pressure [14]. The position of the exhaust valve, determined from measurements, is time-dependent in the model. The in-cylinder pressure from the experiment is used to verify the model's estimated in-cylinder pressure. The exhaust valve lift is measured as the distance from the cylinder cover to the valve edge. The mass of scavenging air flowing through the scavenging ports in each engine cycle is estimated.

2.2. Simulation Setup

Numerical simulations employing computational fluid dynamics (CFD) in a three-dimensional space were conducted by utilizing the ANSYS Forte software package [16-18] between -180 CA and 180 CA. The primary framework of thermo-fluids is guided by governing equations rooted in the conservation law of fluid characteristics. ANSYS Forte utilizes a representation of turbulent reacting flow where the Navier-Stokes equations dictate the fundamental fluid dynamics. The model's transport equations, which are based on the conservation laws of mass, momentum, and

energy, are designed for compressible and gas-phase flows, reflecting the turbulence of the flow [19].

In the field of numerical studies, the model of the computational domain is of paramount importance. The interplay between spray dynamics and the combustion process in internal combustion engines is deeply connected to the necessity of accurate geometric modeling for the numerical examination of combustion events. The full MDE model includes elements such as scavenge port inlets, scavenge ports, the liner of the marine diesel engine, cylinder head, marine diesel injectors, exhaust manifold, exhaust valve stem, exhaust valve seat, and exhaust outlet (Figure 1). This model was constructed using a cross-sectional drawing of the 4T50MX marine diesel test engine, following the guidelines of the project. The two-dimensional cross-sectional drawing of the 4T50MX marine diesel test engine, created using ANSYS Spaceclaim Design Modeler [20], was subsequently scaled up to the actual size in relation to the real cylinder diameter. After this, the model was readied for CFD analysis through the creation of three-dimensional geometry, and surfaces with defined boundary conditions were established within the solid model.



(a)

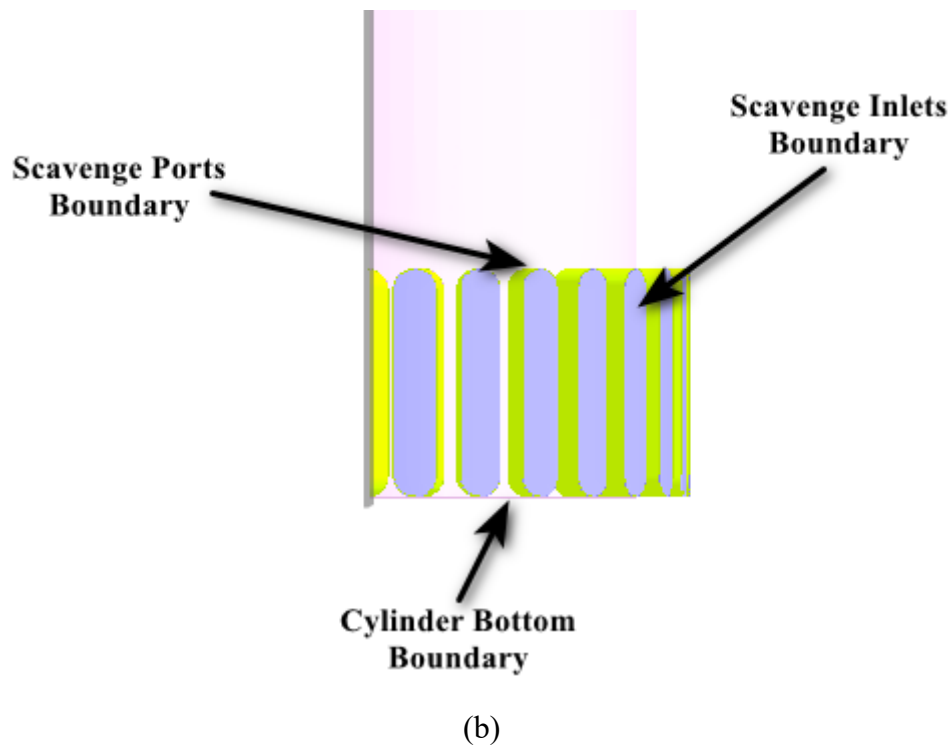


Figure 1. The 3D CFD geometric model of two-stroke MDE [21].

The initial and boundary conditions of the CFD model were presented in Table 2. The simulations commence with the fluid in a state of rest, with the pressure within the domain set to 0.328 MPa, identical to the pressure at the outlet boundary. The temperature within the domain is assigned a value of 312 K, which corresponds to the reference temperature. The fluid will maintain at rest until the pressure exerted from the inlet boundary begins to affect it. The pressure measurements from the scavenging box (P_{sc}) and exhaust receiver (P_{exh}) are chosen as inlet and outlet boundary conditions. The scavenging box pressure, which varies throughout the engine cycle and significantly impacts the volumetric flow through the scavenging port, is chosen as an inlet boundary condition. The average scavenging box pressure is measured as 0.364 MPa. The turbulent length scale for the scavenge inlet boundary is given as 0.5 cm [14]. The turbulent kinetic energy for the scavenge inlet boundary is calculated using turbulence intensity (5%) and turbulent length scale. The outlet pressure boundary uses the measured pressure in the exhaust receiver, with an average value of 0.328 MPa. In this research, it was presumed that the wall boundary conditions were adiabatic. The wall slip condition was selected based on the Law of the Wall, which is typically suggested for turbulent flows. The heat transfer feature was enabled for the moving components, such as the piston and exhaust valve. However, it was not active for the stationary

boundaries, including the cylinder liner, scavenge ports, exhaust manifold, diesel injectors, and cylinder head.

Table 2. Initial and boundary conditions [14, 22].

Initial conditions	
Reference temperature	312 K
Intake reference pressure	0.328 MPa
Intake turbulent kinetic energy	40.6802 m ² /sec ²
Boundary conditions	
Scavenge inlet reference pressure	0.364 MPa
Scavenge inlet turbulence kinetic energy	0.202034 m ² /s ²
Scavenge inlet turbulent length scale	0.5 cm
Outlet reference pressure	0.328 MPa
Piston moving wall temperature	350.0 K
Piston anchored wall temperature	350.0 K
Exhaust valve wall temperature	350.0 K

The Kelvin-Helmholtz and Rayleigh-Taylor (KH-RT) hybrid breakup model was applied to simulate the spray atomization and droplet breakup processes in the solid cone spray model. In addition to this, the unsteady gas jet model [23-25] is selected to eliminate mesh-size dependency for the liquid droplet-ambient gas coupling due to the calculation of the liquid-gas relative velocity in KH-RT hybrid breakup model. A phenomenological model is used to simulate the outcomes of droplet collisions. The adaptive collision mesh model [26] is implemented to simulate fuel droplet collision since it is designed to diminish the mesh dependency and computational cost of droplet collision calculation. The adaptive collision mesh method is based on a pseudo-collision mesh to partition parcels into collision partners. The discrete multi-component (DMC) fuel-vaporization model [27] is used to represent the vaporization of spray droplets. This vaporization model pursues the individual molecules of an actual surrogate fuel during the evaporation process and allows coupling with the reaction kinetics of the individual fuel components. An explicit form of the equation that determines the heat flux from the surrounding gas mixture to the droplet-gas interface is obtained from an approximate solution of the quasi-steady energy equation [28]. The consequence of the collision between the droplet and the wall, depending on the Reynolds number and Weber number of the incident droplet and the surface condition is modeled with the wall impingement model. In engineering applications such as port fuel injection engines, splash is the

most significant and complex regime. The wall splash model by Han et al. [29] was used to model the spray-wall interaction. The O'Rourke and Amsden wall film model [29] was implemented to model liquid film occurred in consequence of sticking, spreading or splashing impingement on the wall. The combustion process in diesel engines are governed by both turbulent mixing dynamics and fuel combustion kinetics. The ignition and combustion chemical kinetics are checked by a complex network of reactions between fuel and air species [28]. The semi-detailed n-heptane reduced chemical kinetic mechanism included 36 species and 74 reactions [30] as alternative fuel for the simulation of marine diesel engines were used in this study. The flame speed model is chosen as Power Law formulation to specify laminar flame speeds [28]. NO_x and soot chemical kinetic mechanisms were integrated in these chemical kinetic mechanisms on the purpose of forecasting NO_x and soot emissions formation.

The accuracy advantages of a Cartesian mesh were compromised by highly distorted cells resulting from moving parts in engine applications. To address these issues, a novel automatic and dynamic meshing technique based on the Arbitrary Lagrangian Euler (ALE) numerical scheme [31] was employed to solve the initial mesh generation problems. An octree structure with perfect cubes in each cell is intended to be the Cartesian mesh in ANSYS Forte. A CAD geometry file that described the actual boundary surfaces of the computational domain was used to create a predefined Cartesian surface mesh. On boundary surfaces that describe boundary conditions, the mesh refinement procedure was used. It's applied dynamically for predetermined time or crank angle intervals using various mesh refinement controls based on various cell sizes. To further refine the surface, these various cell sizes are annotated with the number of cell layers and the proportion of the global mesh size. The study categorized these mesh refinement controls as "Combustion Point Refinement" for injectors, "All Walls" for wall boundaries, "Open Boundaries" for open boundaries like inlets and outlet, and "Valve Stem" and "Valve Seat" for exhaust valve. The mesh refinement controls used in this study are listed in Table 3. For a full-cycle simulation running in parallel on five cores (an Intel I9 9900 K processor), the total and chemistry wall clock times were 122.22 h and 1.71 h, respectively.

Table 3. Mesh refinement controls [32]

Surface refinement controls				
Boundaries	Size of fraction global size	Number of cell layers to extend refinement from surface		Active
All walls	1/4	3		Always
Open boundaries	1/2	2		Always
Squish TDC	1/4	2		During CA interval (from -20 to 30 CA)
Exhaust valve stem	1/2	2		Always
Exhaust valve seat	1/4	2		Always
Feature refinement controls				
Boundaries	Size of fraction global size	Feature Angle	Feature Radius of Influence (mm)	Active
Coarse Feature	1/2	60°	7	Always
Fine Feature	1/4	60°	2	Always
Point refinement controls				
Boundaries	Size of fraction global size	Radius of Application (cm)	Active	
Combustion 1,2,3	1/2	1.5	During CA Interval (from 2 to 20 CA)	

2.3. Governing Equations

2.3.1. Fluid continuity equation

A mixture of distinct gas species or components is used to model the gas-phase working fluids in CFD combustion. Because of molecular diffusion, flow convection, turbulent transport, interactions with fuel sprays, and combustion, this composition varies during engine operation. The continuity equation for the entire gas-phase fluid can be found by adding the equations for each species. This yields the value of Eq. (1).

$$\frac{\partial \bar{\rho}}{\partial t} + \nabla \cdot (\bar{\rho} \tilde{u}) = \dot{\bar{\rho}}^s \quad (1)$$

where $\bar{\rho}$ is density, \tilde{u} the flow velocity vector and $\dot{\bar{\rho}}^s$ is the source term due to spray evaporation.

2.3.2. Momentum conservation equation

Pressure force, convection, turbulent transport, viscous stress, liquid sprays, and body force are all taken into consideration in the fluid's momentum equation. The following equation is taken into consideration for ANSYS Forte [28].

$$\frac{\partial \bar{\rho} \tilde{u}}{\partial t} + \nabla \cdot (\bar{\rho} \tilde{u} \tilde{u}) = -\nabla \bar{p} + \nabla \cdot \bar{\sigma} - \nabla \cdot \Gamma + \bar{F}^S + \bar{\rho} \bar{g} \quad (2)$$

where p is the pressure, \bar{F}^S is the rate of momentum gain per unit volume due to the spray, g is the specific body force, σ is the viscous shear stress, and Γ is the stress that accounts for the effects of ensemble-averaging of the nonlinear convection.

2.3.3. Energy conservation equation

The first law of thermodynamics states that pressure work and heat transfer are necessary to balance the change in internal energy. The effects of turbulent transport, convection, turbulent dissipation, sprays, chemical reactions, and enthalpy diffusion of a multicomponent flow must also be taken into account when solving flow problems involving internal combustion engines. The internal energy transfer as Eq. (3) in the manner mentioned below [28].

$$\frac{\partial \bar{\rho} \tilde{I}}{\partial t} + \nabla \cdot (\bar{\rho} \tilde{u} \tilde{I}) = -\bar{p} \nabla \tilde{u} - \nabla \cdot \bar{J} - \nabla \cdot H + \bar{\rho} \bar{\varepsilon} + \dot{\bar{Q}}^C + \dot{\bar{Q}}^S \quad (3)$$

where I is the specific internal energy, J is the heat flux vector accounting for contributions due to heat conduction and enthalpy diffusion, $\bar{\varepsilon}$ is the dissipation rate of the turbulent kinetic energy, $\dot{\bar{Q}}^C$ and $\dot{\bar{Q}}^S$ are the rate of the turbulent kinetic energy due to chemical heat release and spray interactions, H accounts for the effects of ensemble-averaging or filtering of the convection.

2.3.4. Gas-phase mixture equation of state

For the gas phase mixture, the equation of state relates to the thermodynamic properties of temperature, pressure and density. The equation then also provides relationships for the internal energy. In ANSYS Forte, the ideal gas law applies under the assumption that the mixed gas components follow the Dalton model and is expressed as Eq. (4) [28]:

$$\bar{p} = R_u \bar{T} \sum_k \left(\frac{\bar{\rho}_k}{W_k} \right) \tag{4}$$

where, R_u is the universal gas constant, and W_k is the molecular weight of species k .

2.3.5. Reynolds-Averaged-Navier-Stokes (RANS)

The goal of the Reynolds-Averaged-Navier-Stokes (RANS) method applied in this work is to obtain the ensemble average of the flow field from many flow realizations under comparable circumstances. Large-scale diffusion and turbulent transport and mixing have the same overall average because turbulence affects fluid transport and mixing much more than laminar flow. The main effects of turbulence on the averaged flow and combustion properties are preserved while the RANS technique removes the need to resolve small-scale structures and fluctuations in individual flow realizations. The advanced version of the model is derived from Re-normalized group theory (RNG), as given in Eq. (5) and Eq. (6) [33].

$$\frac{\partial \bar{\rho} \tilde{k}}{\partial t} + \nabla \cdot (\bar{\rho} \tilde{\mathbf{u}} \tilde{k}) = \frac{2}{3} \bar{\rho} \tilde{k} \nabla \cdot \tilde{\mathbf{u}} + (\bar{\boldsymbol{\sigma}} - \Gamma) : \nabla \tilde{\mathbf{u}} + \nabla \cdot \left[\frac{(\mu + \mu_T)}{Pr_k} \nabla \tilde{k} \right] - \bar{\rho} \tilde{\varepsilon} + \dot{W}^s \tag{5}$$

$$\begin{aligned} \frac{\partial \bar{\rho} \tilde{\varepsilon}}{\partial t} + \nabla \cdot (\bar{\rho} \tilde{\mathbf{u}} \tilde{\varepsilon}) = & - \left(\frac{2}{3} c_{\varepsilon 1} - c_{\varepsilon 3} \right) \bar{\rho} \tilde{\varepsilon} \nabla \cdot \tilde{\mathbf{u}} + \nabla \cdot \left[\frac{(\nu + \nu_T)}{Pr_\varepsilon} \nabla \tilde{\varepsilon} \right] \\ & + \frac{\tilde{\varepsilon}}{\tilde{k}} \left[c_{\varepsilon 1} (\bar{\boldsymbol{\sigma}} - \Gamma) : \nabla \tilde{\mathbf{u}} - c_{\varepsilon 2} \bar{\rho} \tilde{\varepsilon} + c_s \dot{W}^s \right] - \bar{\rho} R \end{aligned} \tag{6}$$

Data of the model constants Pr_k , Pr_ε , $c_{\varepsilon 1}$, $c_{\varepsilon 2}$, $c_{\varepsilon 3}$ used in the RNG version are also listed in Table 4 [34]. $c_{\varepsilon 3}$ model constant is given in Eq. (7).

Table 4. Constants in the standard and RNG k - ε models [34].

	C_μ	$C_{\varepsilon 1}$	$C_{\varepsilon 2}$	$C_{\varepsilon 3}$	$1/Pr_k$	$1/Pr_\varepsilon$	η_0	β
Standart k - ε	0.09	1.44	1.92	-1.0	1.0	0.769	-	-
RNG k - ε	0.0845	1.42	1.68	Eq. (3)	1.39	1.39	4.38	0.012

$$c_{\varepsilon 3} = \frac{-1 + 2c_{\varepsilon 2} - 3m(n-1) + (-1)^\delta \sqrt{6} c_\mu c_\eta \eta}{3} \tag{7}$$

2.3.6. Chemical kinetics formulation

The chemical reactions that take place in combustion simulations can be precisely described by chemical kinetic mechanisms. The reaction pathways and corresponding reaction rates that result in the shift in species concentrations are described by these mechanisms. As a result, the general form in Eq. (8) can depict chemical species-related reactions that are either reversible or irreversible in intricate chemical kinetic mechanisms [35].



whereby, the production rate of the k^{th} species in the i^{th} reaction can be written as

$$\dot{\omega}_{ki} = (\nu''_{ki} - \nu'_{ki}) q_i \quad (k = 1, \dots, K) \quad (9)$$

where, q_i is the rate progress of reaction i . The chemical source term $\dot{\rho}_k^c$ in the species continuity equation can be found by adding up $\dot{\omega}_{ki}$ all of the reactions, as shown below:

$$\dot{\rho}_k^c = W_k \sum_{i=1}^I \dot{\omega}_{ki} \quad (10)$$

2.4. Test of Mesh Sensivity

Experimental cylinder pressure data from Ref. [14, 22] was used to validate the model presented in this study. Three mesh cell counts were tested: 607116, 1158702, and 1956754. The cell counts correlate with global mesh sizes of 24, 18, and 15 mm, respectively. Figure 2 shows how different cell numbers affect the comparison of the in-cylinder pressure curves from simulations and experiments.

The computed maximum compression pressure values for the three cell number scenarios are extremely similar to one another, as seen in Figure 2. Based on the recorded maximum compression pressure, the mean absolute percentage errors (%) for the three cases are, however, 12.312, 12.824, and 13.755, respectively. For the cases with 607116, 1158702, and 1956754 cell numbers, the mean absolute percentage errors (%) are set to 5.166, 0.253, and -1.363 when the calculated maximum combustion pressure is compared with the experimental maximum

combustion pressure. The maximum errors converge to 7.29 %, 6.38 %, and 8.53 %, respectively, based on the measured in-cylinder pressure when accounting for all calculated in-cylinder pressure values. Thus, for the simulation studies, the second mesh cell number (1158702) was established. The progression of the optimum mesh cell count and crank angle is depicted in Figure 3. Because of the adaptive mesh refinement control, the mesh cell number for EVO and EVC increased in value. Figure 4 displays the best converged result, which was reached at an 18 mm global mesh size when looking at the in-cylinder pressure history.

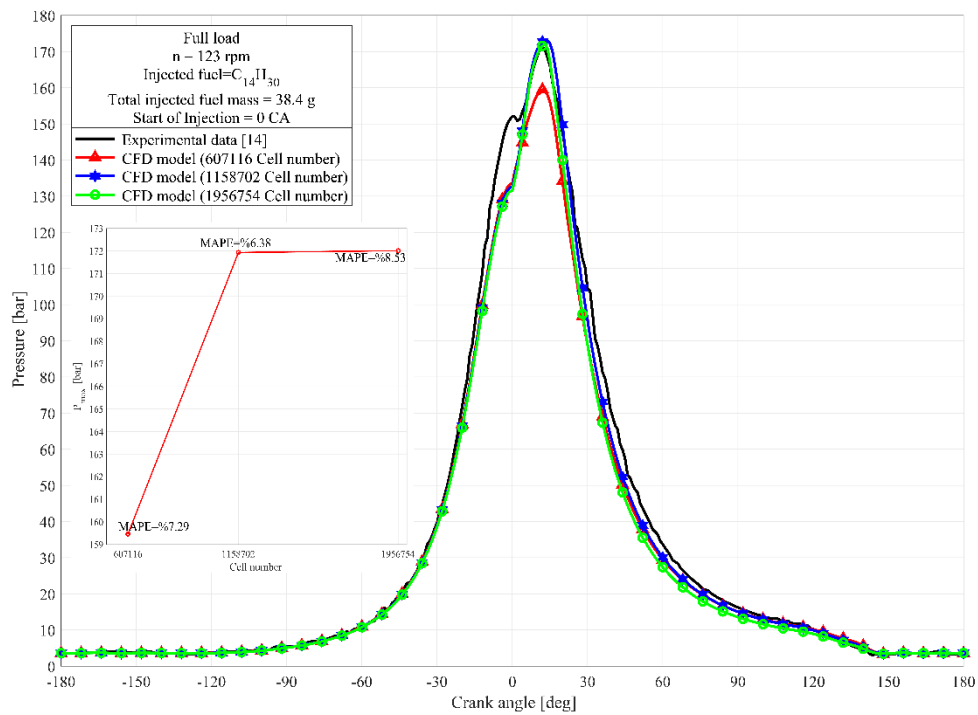


Figure 2. Mesh sensitivity analysis

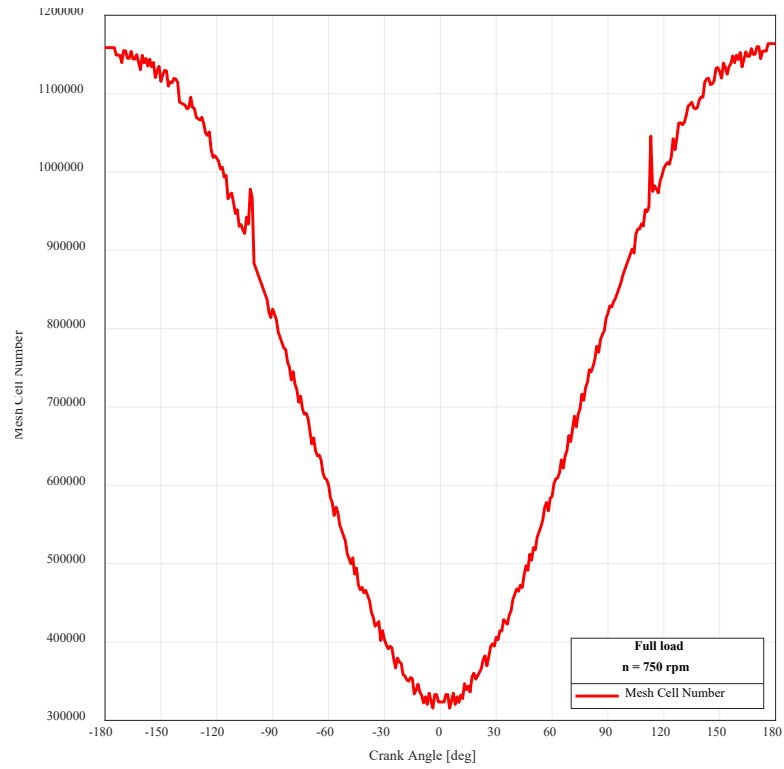


Figure 3. Optimum mesh (1158702) cell number in terms of crank angle

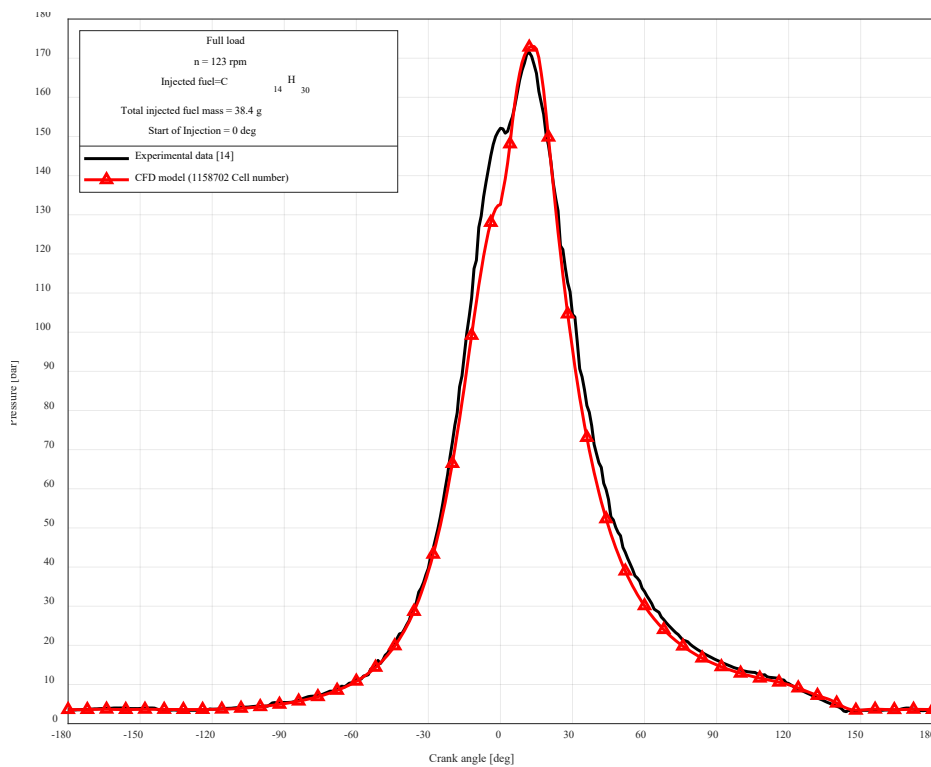


Figure 4. The validation of CFD model for the in-cylinder pressure history

3. RESULTS AND DISCUSSIONS

In this section we present a detailed evaluation of our results.

3.1. Combustion Characteristics

Changes in cylinder pressure with respect to crank angle position for different scavenge air inlet temperatures are shown in Figure 4. The maximum cylinder pressure values that were calculated at scavenge air inlet temperatures of 300, 312, 330, and 340 K are 175.9, 173, 169, and 166.6 bar, respectively. The main factors contributing to decreasing maximum cylinder pressure values are decreased oxygen concentration, increased heat loss, increased thermal stress, and decreased air density [36]. The compression cylinder pressure values at 300, 312, 330 and 340 K scavenge air inlet temperatures are calculated to be 133.4, 132.3, 131, and 130.2 bar, respectively. The reason behind this phenomenon is reduced air density caused by higher temperatures, leading to less oxygen availability for combustion, incomplete fuel-air mixing, longer ignition delays, and an increased likelihood of uncontrolled combustion events like knocking. The rise in the temperature of the inlet charge causes the ignition delay to decrease, which lowers the compression pressure. The pressure level during the combustion process is significantly influenced by the premixed peak. As a result, during the combustion process, the pressure level decreases along with the premixed peak and vice versa.

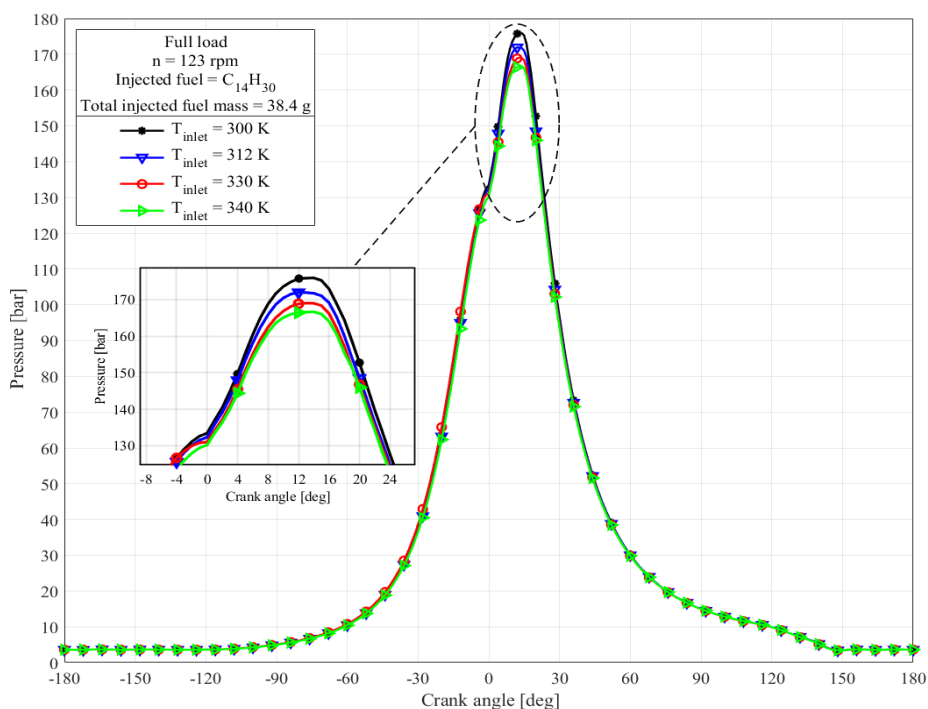


Figure 4. The pressure history for different scavenge air inlet temperatures [32]

For various values of the scavenge air inlet temperature, Figure 5 displays the average temperature inside the cylinder along with the matching crank angle curves. The maximum in-cylinder temperature values are determined to be 1486.9, 1505.6, 1571.3, and 1606.6 K for scavenge air inlet temperatures of 300, 312, 330, and 340 K, as illustrated in Figure 5. This could be explained by the incoming air's higher temperature, which increases the thermal energy inside the cylinder. A more thorough and rapid combustion process is produced by the improved fuel vaporization and more efficient combustion caused by the higher air temperature. Based on calculated scavenge air inlet temperatures of 300, 312, 330, and 340 K, the peak values of the premixed in-cylinder temperature are 810.7, 837.9, 878.9, and 902.5 K, respectively. This phenomenon can be explained by the fact that hotter air at the intake accelerates the fuel vaporization process, improving fuel-air mixing and producing a more homogeneous and flammable mixture. Higher peak temperatures occur during the premixed combustion phase as a result of the enhanced mixture quality and faster, more efficient combustion process brought about by the higher air temperature.

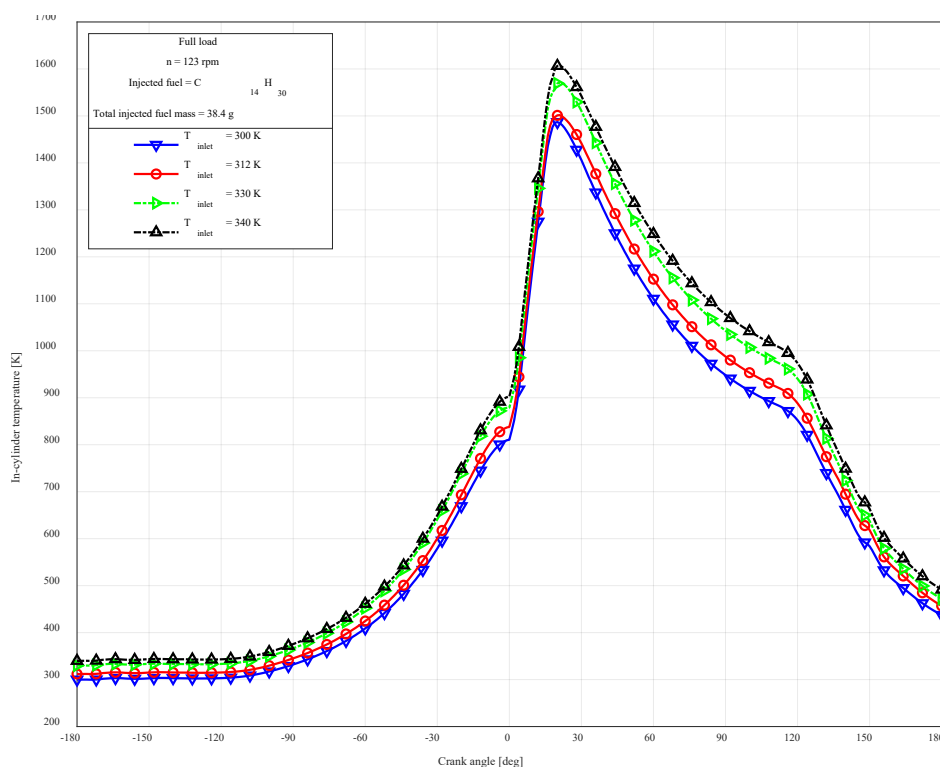


Figure 5. The in-cylinder temperature history for different scavenge air inlet temperatures [32]

The accumulative heat transfer process is shown in Figure 6 for a range of scavenge air inlet temperatures. The final accumulative heat release values are 1584.5, 1579.8, 1581.6, and 1578.2 kJ for scavenge air inlet temperatures of 300, 312, 330, and 340 K, respectively [32]. The highest

values of accumulative heat release are found at 1590.3, 1585.4, 1587.2, and 1583.7 kJ, in that order. This is because the higher temperature of the incoming air causes the combustion process to proceed more quickly, which explains the declining final and maximum cumulative heat release values. This quick combustion causes incomplete combustion and a lower total heat release, which in turn causes lower maximum heat release values within the cylinder. It also shortens the combustion duration and reduces the amount of time for fuel-air mixing. In comparison to the values observed at 300 K inlet temperature for the same, the final and maximum cumulative heat transfer values for scavenge air decrease by 0.42% and 0.39%, respectively, at 340 K inlet temperature.

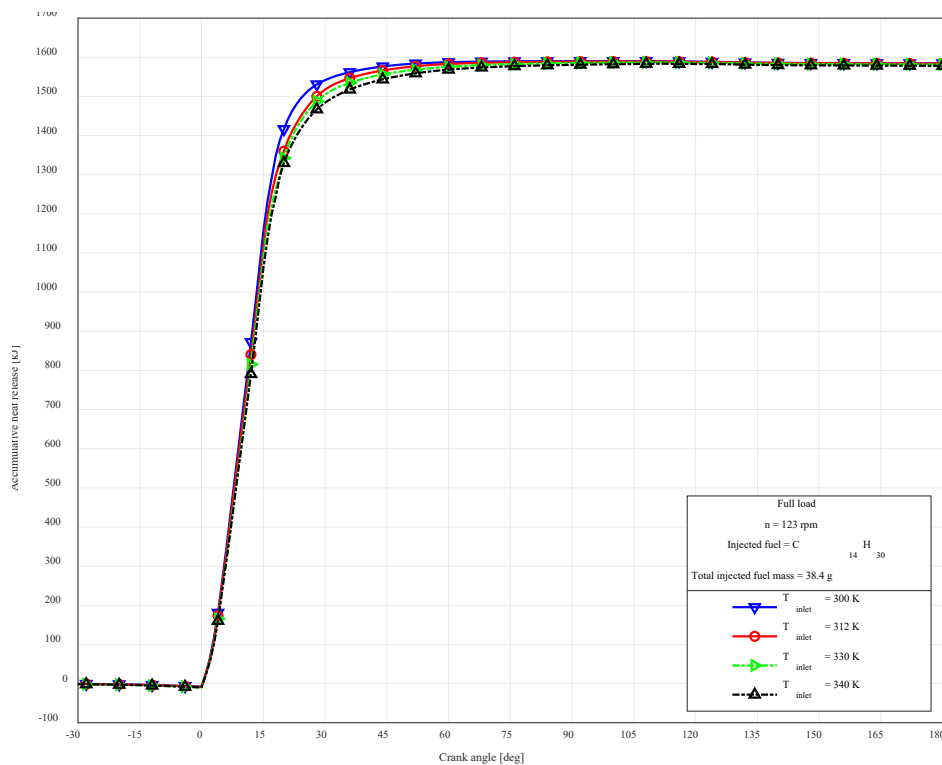


Figure 6. The accumulative heat release history for different scavange air inlet temperatures [32]

3.2. Exhaust Emission Characteristics

The formation of NO_x emissions are based on high combustion temperature and oxygen concentration. The variation of NO_x emissions on crank angle for different scavange air inlet temperature cases is visualized by Figure 7. The maximum NO_x emission values for scavange air inlet temperatures of 300, 312, 330, and 340 K are 1907.2, 1933.3, 2140.8, and 2256.5 ppm, respectively. The final NO_x emission values are obtained at 792.3, 818.3, 853.9, and 918.6 ppm,

respectively. This is due to high combustion temperature which reacts with nitrogen in the air supplied for combustion with increased scavenge air inlet temperature [37]. Another reason is also that the temperature gradient from the exhaust to the scavenge ports is high. This can lead to a higher exhaust back pressure and the possibility of intermixing air and gases, which can further contribute to the increase in NO_x emissions [38].

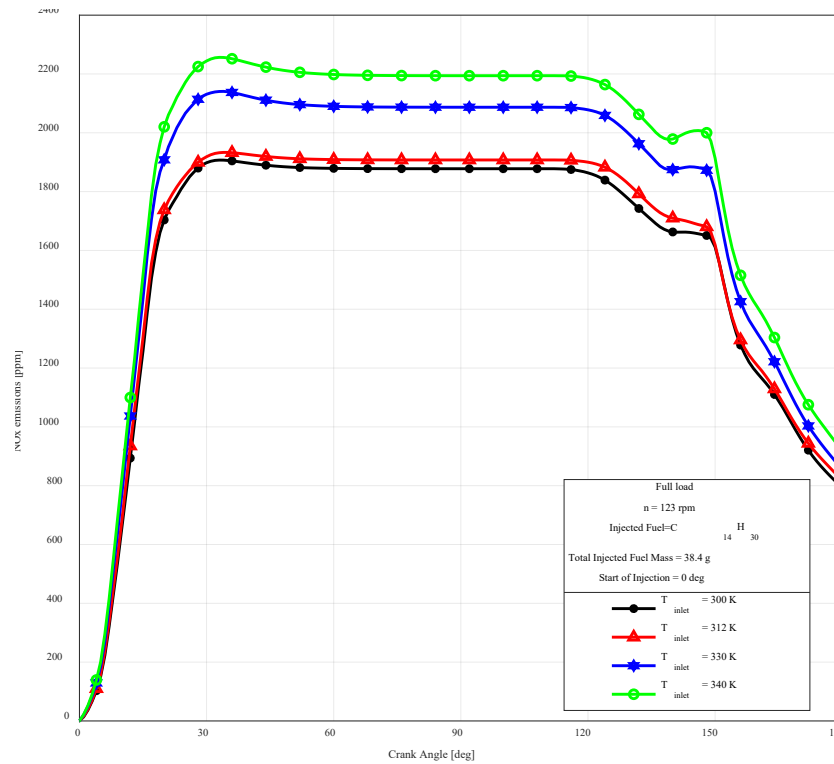


Figure 7. The NO_x emissions crank angle history for different scavange air inlet temperatures

The variation of carbon monoxide (CO) emissions on crank angle for different scavange air inlet temperature cases is visualized by Figure 8. The maximum CO emission values for scavange air inlet temperatures of 300, 312, 330, and 340 K are 14879.3, 16967.3, 19082.9, and 20375.8 ppm, respectively. The rationale behind this is the incomplete combustion, which occurs when there is not enough oxygen to fully oxidize the carbon in the fuel. When the temperature of the scavange air inlet increases, it can lead to a higher mass of escaping fresh air. This increased fresh air inlet cannot compensate for the loss of fresh air, leading to a reduction in the trapped air mass [39]. This reduction in trapped air mass can result in an improper air-fuel mixture, leading to incomplete combustion [19, 40].

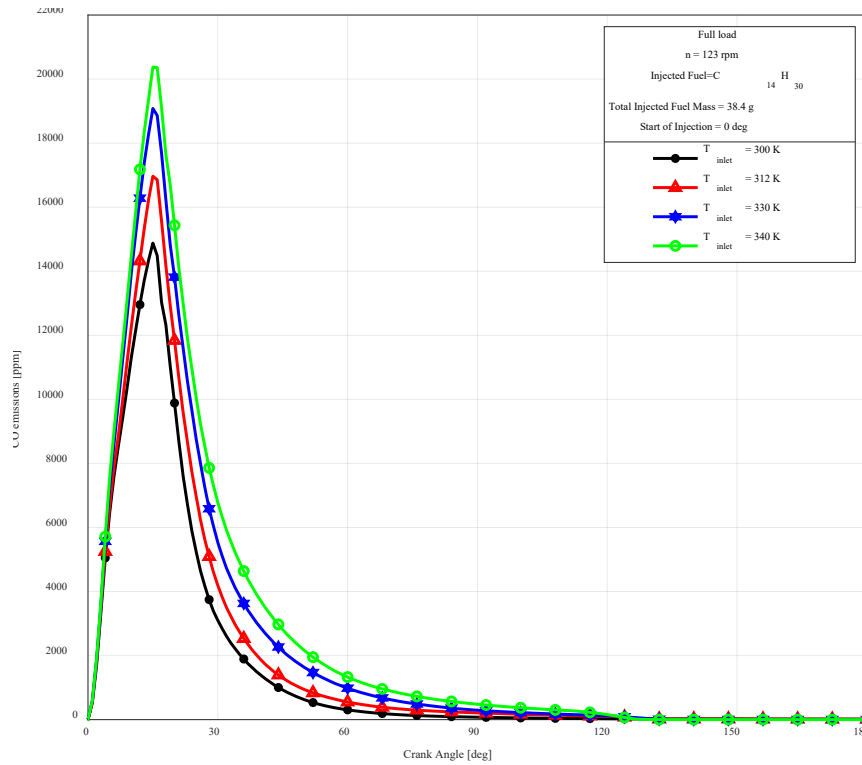


Figure 8. The CO emissions crank angle history for different scavange air inlet temperatures

The variation of unburned hydrocarbon (UHC) emissions on crank angle for different scavange air inlet temperature cases is visualized by Figure 9. The maximum UHC emission values for scavange air inlet temperatures of 300, 312, 330, and 340 K are 2726.1, 3136.4, 3674.3, and 3743.9 ppm, respectively. The reason for this is incomplete combustion. Higher scavange air inlet temperatures can affect air-fuel mixing process, potentially leading to areas of rich or lean mixture, which can result in incomplete combustion and higher UHC emissions [19, 40].

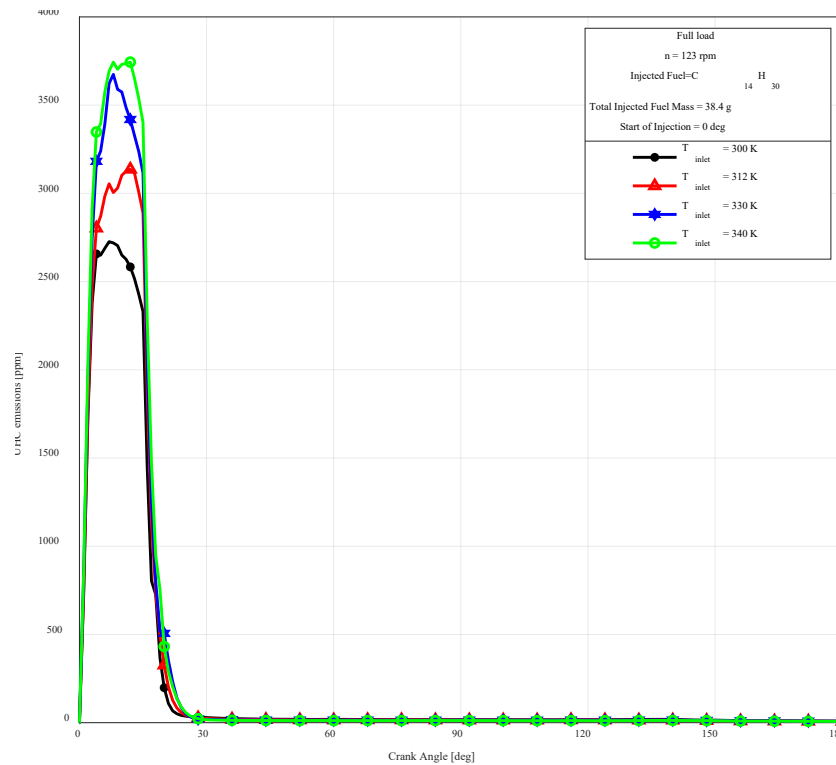


Figure 9. The UHC emissions crank angle history for different scavange air inlet temperatures

4. CONCLUSION

In order to model and analyze the two-stroke MDE, numerical simulation using CFD software was carried out in this study. The cylinder pressure, temperature, heat release rate, and exhaust emissions (NO_x, CO, and UHC) at the optimal mesh case are the evaluated outputs for varying scavange air inlet temperatures. Utilizing the experimental cylinder pressure data, the simulation model was validated. The following is a presentation of the study's key findings:

1. The calculated pressures are in good agreement with the experimental data with regard to cylinder pressure values for three investigated cases. The optimum case was determined as 1158702 cell number (6.38% Mean Absolute Percentage Error). The calculated maximum combustion pressure converges with 0.253% error in regard to the measured maximum combustion pressure.
2. The maximum cylinder pressure values are 175.9, 173, 169 and 166.6 bar when computed at scavange air inlet temperatures of 300, 312, 330, and 340 K. The values of compression cylinder pressure at scavange air inlet temperatures of 300, 312, 330, and 340 K are determined to be 133.4, 132.3, 131 and 130.2 bar, in that order.

3. For scavenge air inlet temperatures of 300, 312, 330, and 340 K, the maximum in-cylinder temperature values are found to be 1486.9, 1505.6, 1571.3, and 1606.6 K. The premixed in-cylinder temperature has peak values of 810.7, 837.9, 878.9, and 902.5 K, in that order.
4. The final accumulative heat release values are 1584.5, 1579.8, 1581.6, and 1578.2 kJ for scavenge air inlet temperatures of 300, 312, 330, and 340 K, respectively. The highest values of accumulative heat release are found at 1590.3, 1585.4, 1587.2, and 1583.7 kJ, in that order.
5. The maximum NO_x emission values for scavenge air inlet temperatures of 300, 312, 330, and 340 K are 1907.2, 1933.3, 2140.8, and 2256.5 ppm, respectively.
6. The maximum CO emission values for scavenge air inlet temperatures of 300, 312, 330, and 340 K are 14879.3, 16967.3, 19082.9, and 20375.8 ppm, respectively.
7. The maximum UHC emission values for scavenge air inlet temperatures of 300, 312, 330, and 340 K are 2726.1, 3136.4, 3674.3, and 3743.9 ppm, respectively.

In the forthcoming study, it will be performed several CFD analysis with the different chemical kinetic mechanism which represents completely physical and chemical characteristics of the heavy fuel oil.

NOMENCLATURE

ALE	: Arbitrary Lagrangian Euler
CA	: Crank angle (degree)
CFD	: Computational fluid dynamics
CO	: Carbon monoxide
DMC	: Discrete multi-component
DWI	: Direct water injection
EGR	: Exhaust gas recirculation
HRR	: Heat release rate
IMO	: International Maritime Organization
KH	: Kelvin – Helmholtz
MDE	: Marine diesel engine
NO _x	: Nitrous oxide emission
OCV	: Ocean-going commercial vessel
RANS	: Reynolds Averaged Navier-Stokes
RNG	: Renormalized group
RT	: Rayleigh – Taylor
SFOC	: Specific fuel oil consumption
UHC	: Unburned Hydrocarbon
WEF	: Water emulsified fuel
k	: Turbulence kinetic energy (m ² /s ²)
ε	: Turbulence dissipation (m ² /s ³)
T _{inlet}	: Scavenge inlet temperature (K)

ACKNOWLEDGMENT

This study is produced from PhD thesis of Enes Fatih Pehlivan at the Department of Naval Architecture and Marine Engineering, The Graduate School of Natural and Applied Sciences, Karadeniz Technical University.

DECLARATION OF ETHICAL STANDARDS

The authors of the paper submitted declare that nothing which is necessary for achieving the paper requires ethical committee and/or legal-special permissions.

CONTRIBUTION OF THE AUTHORS

Enes Fatih Pehlivan: Performed numerical analysis and analyse the results, revise the manuscript.

İsmail Altın: Wrote the manuscript.

CONFLICT OF INTEREST

There is no conflict of interest in this study.

REFERENCES

- [1] Zhu Z, Liang X, Cui L, Wang K, Wang X, Zhu S. Simulation research on the injection strategy of a diesel-ammonia dual-fuel marine engine. *Energy Fuels* 2023; 37(13): 9736–45.
- [2] Liang X, Liu Z, Wang K, Wang X, Zhu Z, Xu C, Liu B. Impact of pilot injection on combustion and emission characteristics of a low-speed two-stroke marine diesel engine. *Energies* 2021; 14(2): 417.
- [3] Cong YJ, Gan HB, Wang HY. Parameter investigation of the pilot fuel post-injection strategy on performance and emissions characteristics of a large marine two-stroke natural gas-diesel dual-fuel engine. *Fuel* 2022; 323: 124404.
- [4] Wei H, Chen X, Wang G, Zhou L, An S, Shu G. Effect of swirl flow on spray and combustion characteristics with heavy fuel oil under two-stroke marine engine relevant conditions. *Applied Thermal Engineering* 2017; 124: 302–14.
- [5] He F, Wei J. Numerical simulation of scavenging process of large 2-stroke marine diesel engine. 2nd International Conference on Automatic Control and Information Engineering, Atlantis Press, 2017.

- [6] Yılmaz H. Assessment of Combustion and Emission Characteristics of Various Gas Mixtures under Different Combustion Techniques. *International Journal of Energy Studies* 2020; 5 (1): 13-41.
- [7] Zhang B, Zhang P, Zhang Z, Yang SS, Wang C, Zeng F. Numerical simulation of flow field characteristics of the cooling water jacket of a marine diesel engine. *7th International Conference on Energy Materials and Environment Engineering (ICEMEE 2021)*, 261, 02040, 2021.
- [8] Menon P, Mittal M. Modeling and simulation of diesel engines using CFD and its applications in optimizing various in-cylinder techniques. In: Agarwal, A.K., Kumar, D., Sharma, N., Sonawane, U. (eds) *Engine Modeling and Simulation. Energy, Environment, and Sustainability*. Springer, Singapore, 2021; 89-143.
- [9] Chryssakis C, Kaiktsis L, Frangopoulos A. Computational investigation of in-cylinder NO_x emissions reduction in a large marine diesel engine using water addition strategies. *SAE Technical Paper Series 2010*; Paper no: 2010-01-1257.
- [10] Liu H, Zhang H, Wang H, Zou X, Yao M. A numerical study on combustion and emission characteristics of marine engine through miller cycle coupled with EGR and water emulsified fuel. *SAE Technical Paper Series 2016*; Paper no: 2016-01-2187.
- [11] Yang R, Theotokatos G, Vassalos D. CFD modelling and numerical investigation of a large marine two-stroke dual fuel direct injection engine. *Ships and Offshore Structures* 2022; 17 (5): 1062–1074.
- [12] Senčić T, Mrzljak V, Medica-Viola V, Wolf I. CFD analysis of a large marine engine scavenging process. *Processes* 2022; 10 (1): 141.
- [13] Mavrelou C, Theotokatos G. Numerical investigation of a premixed combustion large marine two-stroke dual fuel engine for optimising engine settings via parametric runs. *Energy Conversion and Management* 2018; 160: 48-59.
- [14] Sigurdsson E. Scavenging flow in a two-stroke diesel engine. MSc Thesis, Technical University of Denmark, 2011.
- [15] Woodyard D. *Pounders Marine Diesel Engines and Gas Turbines*. Elsevier Butterworth-Heinemann, 8th edition, 2004.
- [16] Hafiz MNM, Hairuddin AA, Md Rezali KA, Masuri SU, Mossa MAA. Numerical study of piston bowl geometries on PFI-HCCI engine performance. *Journal of Mechanical Engineering and Sciences* 2023; 17 (4): 9689-9699.
- [17] Ghazal OH. Reducing Diesel Engine Emission using Reactivity Controlled Approach. *Journal of Ecological Engineering* 2018; 19 (1): 94-103.

- [18] Altun Ş, Firat M, Okcu M. Numerical Analysis on the Effect of Hydrogen as Low-Reactivity Fuel in a 3D Scanned Engine Model Operated on RCCI Mode. *Arabian Journal for Science and Engineering* 2023; 48: 11545–11557.
- [19] Rahman KM, Ahmed Z. Combustion and Emission Characteristics of a Diesel Engine Operating with Varying Equivalence Ratio and Compression Ratio - A CFD Simulation. *Journal of Engineering Advancements* 2020; 1 (3): 100-110.
- [20] Ortiz-Imedio R, Ortiz A, Ortiz I. Comprehensive analysis of the combustion of low carbon fuels (hydrogen, methane and coke oven gas) in a spark ignition engine through CFD modeling. *Energy Conversion and Management* 2022; 251: 114918.
- [21] Pehlivan EF. Exergy analysis based on computational fluid dynamics of a two-stroke marine diesel engine. PhD Thesis, Karadeniz Technical University, 2022.
- [22] Sigurdsson E, Ingvorsen KM, Jensen MV, Mayer S, Matlok S, Walther JH. Numerical analysis of the scavenge flow and convective heat transfer in large two-stroke marine diesel engines. *Applied Energy* 2014; 123: 37-46.
- [23] Abani N, Kokjohn S, Park SW, Bergin M, Munnannur A, Ning W, Sun Y, Reitz RD. An improved spray model for reducing numerical bibliomiscmeter dependencies in diesel engine CFD simulations. *SAE Technical Paper Series* 2008; Paper no: 2008-01-0970.
- [24] Reitz RD. Modeling atomization processes in high-pressure vaporizing sprays. *Atomization and Sprays* 1987; 3: 309-337.
- [25] Yang C, Takamoto Y, Okajima A, Obokata T, Long W. Comparison of computed and measured high-pressure conical diesel sprays. *SAE Technical Paper Series* 2000; Paper no: 2000-01-0951.
- [26] Hou S, Schmidt DP. Adaptive collision meshing and satellite droplet formation in spray simulations. *International Journal of Multiphase Flow* 2006; 32: 935-956.
- [27] Ra Y, Reitz RD. A vaporization model for discrete multi-component fuel sprays. *International Journal of Multiphase Flow* 2009; 35: 101-117.
- [28] ANSYS Inc., ANSYS Forte 2020 R1 Theory Manual.
- [29] Han Z, Xu Z, Trigui N. Spray/wall interaction models for multidimensional engine simulation. *International Journal of Engine Research* 2000; 1(1): 127-146.
- [30] Patel A., King SC., Reitz RD. Development and validation of a reduced reaction mechanism for HCCI engine simulations. *SAE Technical Paper Series* 2004; Paper no: 2004-01-0558.

- [31] Liang L, Shelburn A, Wang C, Hodgson D, Meeks E. A New automatic and dynamic mesh generation technique based on immersed boundary method. International Multidimensional Engine Modeling User's Group Meeting, Detroit, Michigan, 2011.
- [32] Pehlivan EF, Altın, İ. Exergy analysis under consideration of operational parameters by numerical approach in a two-stroke marine diesel engine. *Fuel* 2024; 368: 131650.
- [33] Han Z, Reitz RD. Turbulence modeling of internal combustion engines using RNG $k-\epsilon$ models. *Combustion Science and Technology* 1995; 106: 267-295.
- [34] Tan Z. Multi-dimensional modeling of ignition and combustion in premixed and DIS/CI (direct injection spark/compression ignition) engines. PhD Thesis, University of Wisconsin-Madison, 2003.
- [35] ANSYS Inc., ANSYS Chemkin-Pro Theory Manual. 2022, USA.
- [36] He X, Tan Q, Wu Y, Wei C. Optimization of marine two-stroke diesel engine based on air intake composition and temperature control. *Atmosphere* 2022; 13(2): 355.
- [37] Lu D, Theotokatos G, Zhang J, Zeng H, Cui K. Comparative Assessment and Parametric Optimisation of Large Marine Two-Stroke Engines with Exhaust Gas Recirculation and Alternative Turbocharging Systems. *Journal of Marine Science and Engineering* 2022; 10 (3): 351.
- [38] He X, Tan Q, Wu Y, Wei C. Optimization of Marine Two-Stroke Diesel Engine Based on Air Intake Composition and Temperature Control. *Atmosphere* 2022; 13 (2): 355.
- [39] Ceylan BO. Investigation of seasonal effects on two-stroke marine diesel engine performance parameters and emissions. *Journal of Marine Science Applications* 2023; 22: 795-808.
- [40] Nemati A, Ong JC, Jensen MV, Pang KM, Mayer S, Walther JH. Numerical Study of the Scavenging Process in a Large Two-Stroke Marine Engine Using URANS and LES Turbulence Models. SAE Technical Paper Series 2020; Paper no: 2020-01-2012.